SOFT ROBOTS

Electro-ribbon actuators and electro-origami robots

Majid Taghavi[1,2]*, Tim Helps[1,2]*, Jonathan Rossiter[1,2†]

Origami has inspired novel solutions across myriad fields from DNA synthesis to robotics. Even wider impact can be achieved by active origami, which can move and change shape independently. However, current active origami and the materials that power it are both limited in terms of strength, speed, and strain. Here, we introduce an electrostatic active origami concept, electro-origami, that overcomes these limitations and allows for simple, inexpensive, lightweight, efficient, powerful, and scalable electronic actuators and lightweight and thin robots. The simplest embodiment of electro-origami, electro-ribbon actuators, can be easily fabricated from any combination of conducting and insulating material. We present electro-ribbon actuators that can lift 1000 times their own weight, contract by 99.8% of their length, and deliver specific energy and specific power equivalent to muscle. We demonstrate their versatility in high-stroke and high-force morphologies, multiactuator lattices, 3D-printed and paper actuators, self-twisting spirals, and tensile elements inspired by spider silk. More complex electro-origami devices include solenoids, adaptive grippers, robotic cilia, locomoting robots, self-packing deployable structures, origami artificial muscles, and dynamic origami art.

INTRODUCTION

Origami has been applied to multiple fields, including DNA synthesis (*1*), microfluidics (*2*), biomedical applications, electric batteries (*3*), robotics (*4*), manufacturing, and space structures (*5*). Active origami, whereby independent motion is driven by internally generated forces, allows for even greater applicability, enabling self-deploying biomedical devices (*6*) and novel artificial muscles (*7*, *8*). Various actuation technologies can deliver forces for active origami (*6*–*12*); however, the limitations of these actuation phenomena have resulted in active origami structures that are weak, slow to cycle, strain-limited, or not made from thin materials. Here, we introduce an electrostatic active origami concept that overcomes these limitations and delivers strong and dynamic electro-origami structures made from any combination of conducting and insulating materials.

Electrostatic forces have the potential to be extremely large: As Feynman *et al.* (*13*) eloquently put it, electric force is "about a billion-billion-billion-billion" times stronger than gravitational force. Actuators driven by electrostatic forces are characterized by high efficiencies, fast response times, and low power requirements. Comb drive actuators, for example, have been used for decades in microelectromechanical systems devices (*14*), but the stroke of these actuators is on the order of micrometers (*15*). Larger displacements can be achieved through the use of zipping structures, whereby one electrode incrementally deforms toward a counterelectrode (*16*–*18*); however, when these actuators have been built at the macroscale, the forces they have been able to exert have been limited (*19*–*21*). Liquid-amplified electrostatic actuators have demonstrated high actuation forces, showing the potential of electrostatic zipping (*22*, *23*). In particular, hydraulically amplified electrostatic actuators have used liquid-amplified electrostatic forces to deliver fluid pressure in flexible fluidic actuators (*22*, *24*); however, when made into working devices, their contractions are theoretically limited to less than 18%, and their nonplanar actuation prevents their use in origami structures (*25*). Electro-origami actuators are fundamentally different from these actuators, being driven by purely electrostatic forces with no hydraulic behavior, requiring markedly less liquid dielectric and no encapsulation, allowing for fast, simple fabrication and radically different actuating morphologies, and delivering contractions exceeding 99%.

RESULTS

Electro-origami principle [dielectrophoretic liquid zipping (DLZ)]

The fundamental principle of electro-origami is an origami fold whose opposing sides are oppositely charged (Fig. 1A and fig. S1A). At the fold hinge, a strong electric field is developed (fig. S1B), and an electrostatic force is exerted. This electrostatic force is typically not great enough to do useful work or even cause visible movement. However, if a small bead of high-permittivity, high–breakdown strength liquid dielectric is added at the hinge, then it considerably amplifies the electrostatic force and causes the hinge to close (Fig. 1, A and B, and movie S1), with the liquid dielectric being driven along as the hinge closes. The overall closing force is coupled to Maxwell pressure, $P \propto \varepsilon E^2$, where ε is the dielectric permittivity and E is the electric field (*26*). The liquid dielectric has two complementary effects: First, it increases closing force in proportion to its permittivity relative to air. In addition, its breakdown strength is considerably higher than the breakdown strength of air. Hence, the addition of liquid dielectric allows higher electric fields to be sustained because of its higher breakdown strength, greatly increasing maximum closing force by a factor of $\left(\frac{E_{\text{breakdown,liquid}}}{E_{\text{breakdown,air}}}\right)^2$. Here, silicone oil was used as the liquid dielectric, whose permittivity and breakdown strength are roughly 2.7 and 6.7 times greater than air, respectively, implying that maximum closing force could be increased up to 120-fold.

Serendipitously, as the electro-origami fold closes, the amplifying liquid dielectric bead is kept in place by dielectrophoretic forces (*27*), which have the effect of drawing high-permittivity materials (in this case, the liquid dielectric) into regions of high electric field density (the electro-origami hinge) (*28*). In this manner, a strong closing force is generated throughout actuation using only a single bead of liquid dielectric, which greatly reduces device mass compared with fully submerged or encapsulated solutions (in experiments, a liquid bead provided 92% of the electrostatic force compared with a fully submerged system). This zipping behavior, whereby dielectrophoretic forces retain a bead of liquid dielectric as it amplifies electrostatic zipping, may be called dielectrophoretic liquid zipping (DLZ).

[1]Department of Engineering Mathematics, University of Bristol, Bristol BS8 1QU, UK. [2]Bristol Robotics Laboratory, Bristol BS16 1QY, UK.
*These authors contributed equally to this work.
†Corresponding author. Email: jonathan.rossiter@bristol.ac.uk

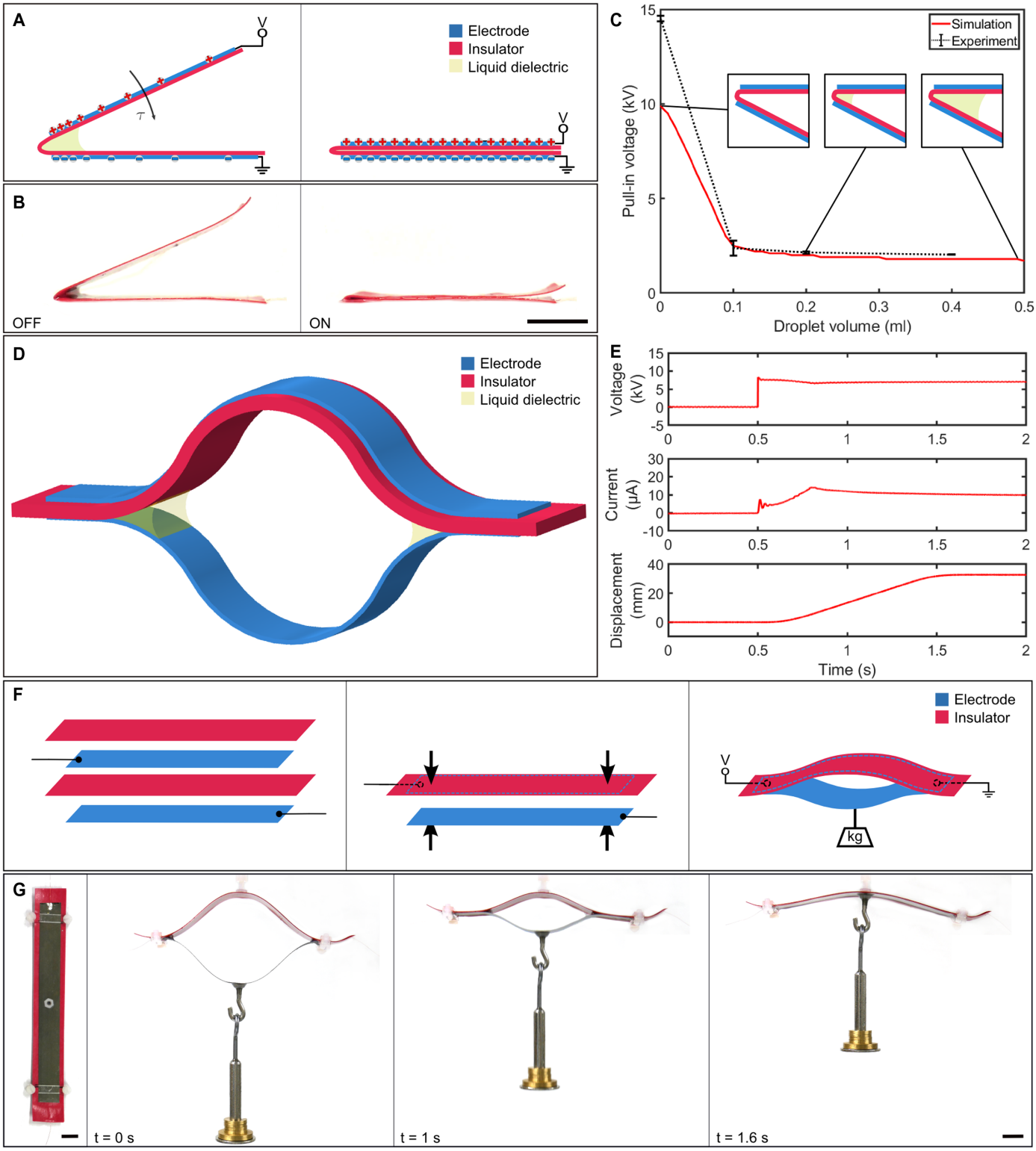

Fig. 1. Electro-origami and electro-ribbon actuator concept. (**A**) Diagrams of actuated electro-origami fold, with charge distribution. (**B**) Photographs of actuated electro-origami fold. (**C**) Effect of droplet volume on pull-in voltage for a zipping electro-origami fold. (**D**) Diagram of electro-ribbon actuator. (**E**) Voltage, current, and displacement during isotonic actuation of an electro-ribbon actuator. (**F**) Manufacture of standard electro-ribbon actuators. (**G**) Photographs of standard electro-ribbon actuator, which is made from thin steel electrodes and PVC tape: plan view and lifting a 20-g mass. Scale bars, 10 mm.

Modeling

We developed a mathematical model to investigate the effect of the bead of liquid dielectric on the behavior of this system (see the Supplementary Materials). For two parallel charged plates separated by an insulator and a medium (fig. S2A), when the insulator is adhered to the insulator-adjacent electrode, the attractive force on the electrodes is given by

$$F = \frac{\frac{1}{2}\varepsilon_{\text{medium}}\varepsilon_0 A V^2}{\left(\frac{\varepsilon_{\text{medium}}}{\varepsilon_{\text{insulator}}} t_{\text{insulator}} + t_{\text{medium}}\right)^2} \quad (1)$$

where F is the attractive force; $\varepsilon_{\text{medium}}$, ε_0, and $\varepsilon_{\text{insulator}}$ are the permittivity of the medium, free space, and the insulator, respectively; A is the plate area; V is the applied voltage; and $t_{\text{insulator}}$ and t_{medium} are the insulator and the medium thickness, respectively. If the insulator is considerably thinner than the medium ($t_{\text{insulator}} \ll t_{\text{medium}}$), the attractive force tends toward

$$F = \frac{\frac{1}{2}\varepsilon_{\text{medium}}\varepsilon_0 A V^2}{{t_{\text{medium}}}^2} \quad (2)$$

which is equivalent to the attractive force between two parallel charged plates separated by a medium only. In contrast, if the medium is considerably thinner than the insulator ($t_{\text{medium}} \ll t_{\text{insulator}}$), the attractive force tends toward

$$F = \frac{\frac{1}{2}\varepsilon_0 A V^2}{\varepsilon_{\text{medium}}\left(\frac{t_{\text{insulator}}}{\varepsilon_{\text{insulator}}}\right)^2} \quad (3)$$

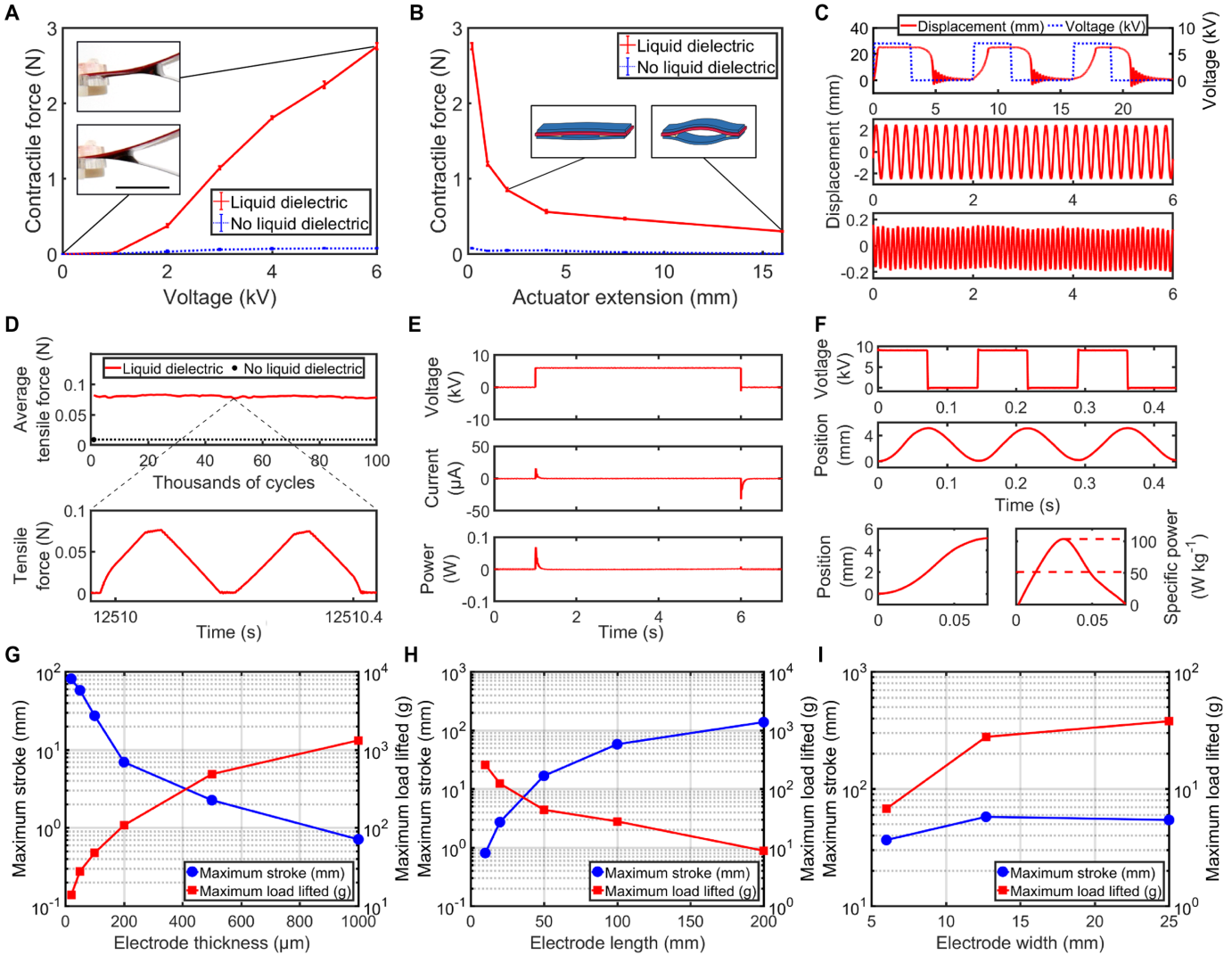

Fig. 2. Electro-ribbon actuator characterization. (**A**) Isometric tensile force at 0.1-mm actuator extension. (Insets) Electro-origami zipping. (**B**) Isometric tensile force at an applied voltage of 6 kV, with inset diagrams showing extension state. Points in (A) and (B) are averages of five trials for one sample, and error bars show SD between trials; intersample variance was low (fig. S4, D and E). (**C**) Bandwidth testing, showing full-amplitude contraction at 0.125 Hz and partial-amplitude oscillation at 5 and 10 Hz. (**D**) Cyclic testing over 100 thousand cycles. (**E**) Voltage, current, and electrical power traces during an experiment to measure efficiency. (**F**) Mechanical power output testing. The peak and average specific powers were 103.51 and 51.45 W kg^{-1}, respectively. (**G** to **I**) Electro-ribbon actuator maximum stroke and load lifted variation with electrode thickness, length, and width, respectively. Scale bar, 10 mm.

In the case of electro-origami, the medium (liquid dielectric or air) thickness ranges smoothly from zero at the fold hinge to considerably larger than the insulator thickness. Such a system cannot be solved analytically, so we developed a finite element model of a zipping electro-origami fold based on Eq. 1 and Euler-Bernoulli beam theory (figs. S2, B and C, and S3, and the Supplementary Materials). The model confirms that only a small droplet of liquid dielectric is required to achieve considerable force amplification: A tiny bead of only 0.2 ml reduced pull-in voltage by more than 80%, asymptotically approaching the fully submerged pull-in voltage of 1700 V (Fig. 1C and the Supplementary Materials). Experimental results for an identical system (fig. S1C) confirmed the validity of the model (Fig. 1C).

Characterization

Fundamentally, electro-origami allows high-strength zipping actuation of prefolded origami structures, enabling a whole range of active origami designs. To characterize the actuation properties of the electro-origami concept in a working device, we began with a simple practical embodiment, the electro-ribbon actuator (Fig. 1D), that comprised two electrodes and a single insulator. When voltage was applied to an electro-ribbon actuator, the opposing electrodes were charged, and the actuator contracted (Fig. 1E). Electro-ribbon actuators could be easily fabricated by using any combination of flexible insulating and flexible conductive material, including indium-tin-oxide (ITO)–coated polyethylene terephthalate (PET), polyimide, graphene-loaded and pure polylactic acid (PLA), and pencil and office paper (table S1).

Our standard actuator used thin steel electrodes and polyvinyl chloride (PVC) tape (Fig. 1F). When electro-ribbon actuators contracted fully, contraction approached 100% because of their extremely low thickness when contracted (Fig. 1G and movie S2). Actuation time was affected by applied voltage (fig. S4A) and load (fig. S4B): Higher voltages sustained stronger fields, which increased the contraction speed of the actuator. Lighter loads decreased the electro-origami hinge angle, which similarly increased field strength, increasing contraction speed. Figure 2 (A and B) shows results from isometric testing of a standard electro-ribbon actuator (experimental setup as shown in fig. S4C); addition of a small bead (around 0.2 ml) of liquid dielectric at each electro-origami fold hinge markedly increased contractile force by a factor of up to 37.

We demonstrated full-amplitude cyclic actuation at a bandwidth of 0.125 Hz (Fig. 2C and movie S3). Higher-frequency operation can be achieved if a lower-amplitude stroke is acceptable: We demonstrated 5-Hz cyclic operation at 9.7% of full amplitude and 10-Hz cyclic operation at 0.62% of full amplitude (Fig. 2C). The charging time of electro-origami actuators was extremely fast and did not notably limit bandwidth; bandwidth limitation was dominated by mechanical inertia,

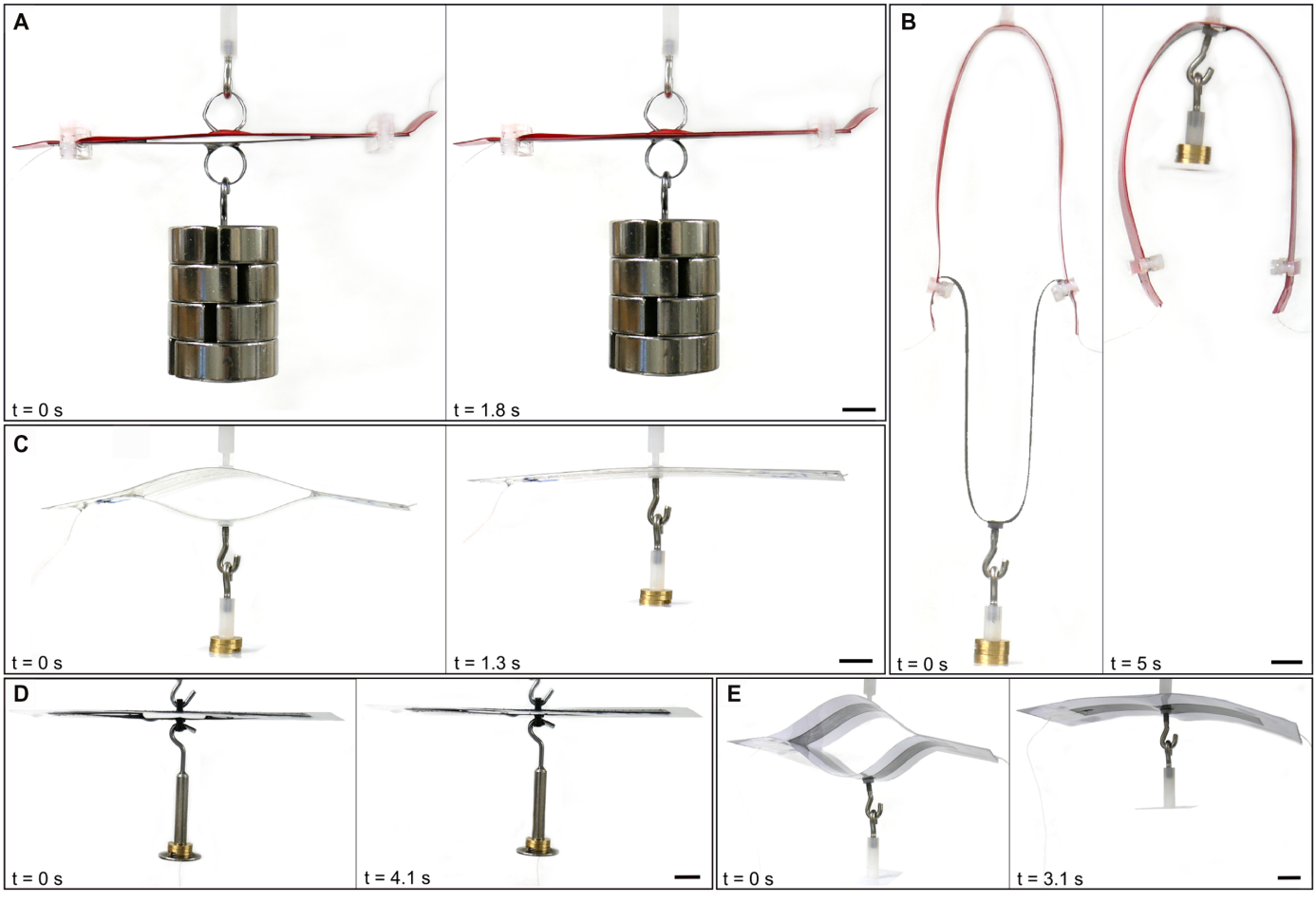

Fig. 3. Electro-ribbon actuators made with different stiffness and from different materials. (**A**) A high-stress actuator lifting 410 g. (**B**) A high-stroke actuator lifting 10.75 g. (**C**) Electro-ribbon actuator made from ITO-coated PET lifting a 5-g mass. (**D**) A 3D printed electro-ribbon actuator, featuring 3D-printed graphene-loaded PLA conductors and a 3D-printed pure PLA insulator. (**E**) Electro-ribbon actuator made from pencil and paper lifting a 3-g mass. Scale bars, 10 mm.

adhesive and cohesive forces, and the availability of liquid dielectric. As suggested by the model (Fig. 1C), as long as a small quantity of liquid dielectric remains at the electro-origami fold hinge, performance is high. However, if all the liquid leaks away, then performance is impaired. For long-term actuation, this can be easily addressed by adding features to retain the liquid dielectric between cycles. For example, we investigated surface structure modifications: perpendicular channel-shaped cutouts in the insulator layer that act as liquid reservoirs. An actuator modified in this manner delivered 100,000 isometric actuation cycles with negligible variation in force (Fig. 2D). After 100,000 cycles, the actuation force exerted was still roughly 10 times greater than the force when no liquid dielectric was present.

Table 1. Dimensions, masses, actuator contractions, and descriptions of steel PVC electro-ribbon actuators. In all electro-ribbon actuators, the electrode width was 12.7 mm, and the insulator consisted of two layers of 130-μm-thick PVC tape.

	Electrode length (mm)	Electrode thickness (mm)	Conductor and insulator mass (g)	Actuator contraction (%)	Description
Standard	100	50	2.28	99.38	
High force	100	1000	25	23.93	Actuator force: 12.91 N
High stress	10	100	0.9	33.91	Stress: 40.77 kPa
High contraction	200	20	2.95	99.84	Contraction: 99.84%
High-contraction rate	100	500	13.2	81.48	Average contraction rate: 1161% s^{-1} Peak contraction rate: 1985% s^{-1}
High specific force	10	50	0.36	17.05	Specific force: 10164.25 N kg^{-1}
High specific energy	100	50	2.28	99.38	Specific energy: 6.8809 J kg^{-1}
High specific power	100	500	13.2	81.48	Average specific power: 51.45 W kg^{-1} Peak specific power: 103.41 W kg^{-1}
High energy density	10	50	0.63	68.97	Energy density: 44.17 kJ m^{-3}
High power density	100	500	13.2	81.48	Average power density: 424.45 kW m^{-3} Peak power density: 853.83 kW^{-1}
Prebent	70	70	2.24	96.30	

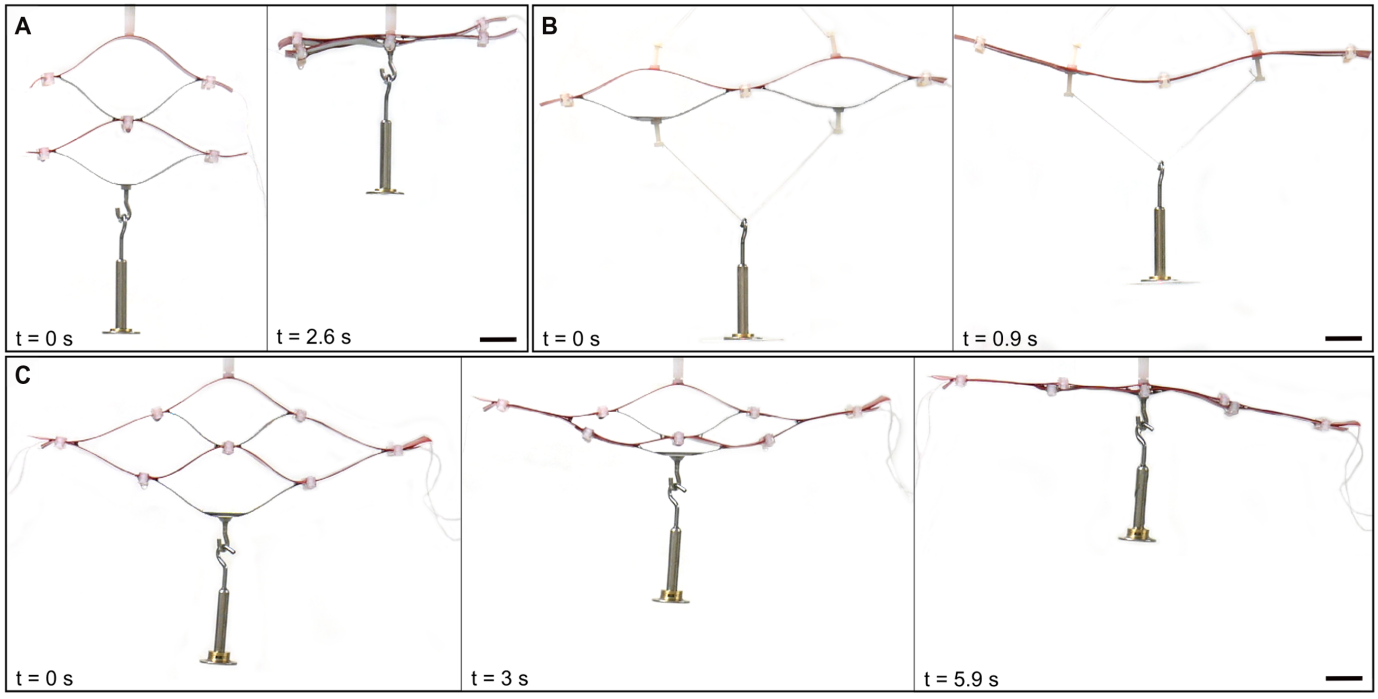

Fig. 4. Electro-ribbon actuators integrated into multiactuator structures. Series (**A**), parallel (**B**), and lattice (**C**) configurations of electro-ribbon actuators. Scale bars, 20 mm.

Insulator charging can be an issue for zipping actuators, whereby charge can become trapped between cycles; however, we did not observe any variation in performance during these 100,000 cycles that could be attributed to the effects of charging. One explanation for this is that the lower permittivity of the liquid dielectric (2.7) compared with the insulator (4.62) reduces the field sustained in the insulator layer. The efficiency of electrostatic actuators is typically high, in the region 60 to 90% (*29*); although this was not explicitly studied for electro-ribbon actuators, the highest recorded was 69.67% (Fig. 2E).

The morphology of electro-ribbon actuators presents a large design space. Figure 2 (G to I) shows the effect of varying the dimensions of an electro-ribbon actuator's two electrodes. Because electro-ribbon actuators are composed of a pair of steel electrodes, which are deflected by an external load, they act as tension springs, exerting a tensile force that monotonically increases with extension. The effect of electrode dimension on stroke and load is tied to their bending stiffness, which is influenced by thickness, length, and width, according to beam theory. Increasing electrode thickness and width increases the second moment of area of the beam, which increases its flexural rigidity EI, where E is Young's modulus and I is second moment of area. Reducing the beam length reduces the moment induced by loading, reducing deflection. Hence, stiffer, shorter beams tend to deflect less under load (reducing available stroke), and the reduced deflection implies a stronger electric field and, accordingly, larger electrostatic force. Results from simulation of the effect of electrode morphology for a single electro-origami fold (fig. S5, B to D) show qualitative agreement with Fig. 2 (G to I), with the same relationships observed between (i) thickness, length, and width and (ii) stroke and load.

By investigating the effects of electrode dimension on output parameters, we gained an understanding for how specific performance characteristics could be increased. Using these findings, we created a high-stress actuator that achieved a maximum actuation stress of 40.76 kPa. Despite lifting 527.75 g, more than 500 times its mass, contraction remained high at 33.91%. Figure 3A and movie S4A show a similar high-stress actuator lifting 410 g. A high–specific force actuator could lift 373 g, more than 1000 times its mass, while contracting by 17.05%. We created a high-stroke, high-contraction actuator that achieved a stroke of 181.92 mm (Fig. 3B and movie S4B), shortening by an impressive 99.84%. This is the highest contraction we are aware of for contracting actuated structures. The highest recorded average contraction rate was 1161% s^{-1}, and peak contraction rate was 1985% s^{-1}. The highest recorded specific energy and specific power were 6.88 J kg^{-1} and 103.51 W kg^{-1}, respectively (Fig. 2F and movie S5), similar to the performance of mammalian muscle (typically, 8 J kg^{-1} and 50 W kg^{-1}) (*30*). The highest recorded energy density and power density were 44.17 kJ m^{-3} and 853.83 kW m^{-3}, respectively. These performance characteristics are summarized in Table 1, which also provides structural properties of the electro-ribbon actuators in question. In comparison with typical performance characteristics for selected previously investigated electroactive actuator structures, electro-origami delivers stress of the order of muscle [muscle, 0.1 MPa; HASEL (hydraulically amplified self-healing electrostatic), 0.032 to 0.3 MPa (*24*); dielectric elastomer, 1.6 MPa (*30*); Peano-HASEL, 6 MPa (*25*)], considerably higher contraction than previous technology [Peano-HASEL, 10%; muscle, 20%; multilayer dielectric elastomer, 46% (*31*)], specific energy similar to muscle (muscle, 8 J kg^{-1}; HASEL, 70 J kg^{-1}; dielectric elastomer, 150 J kg^{-1}), and specific power similar to previous technology (muscle, 50 W kg^{-1}; Peano-HASEL, 160 W kg^{-1}; and dielectric elastomer, 500 W kg^{-1}).

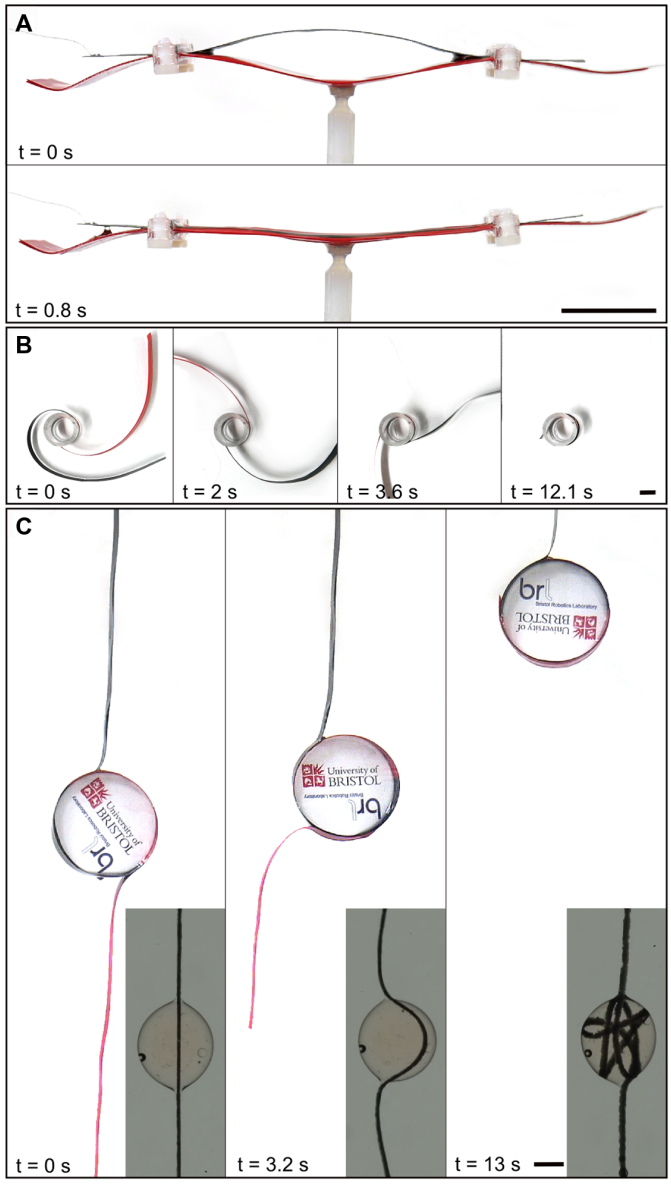

Fig. 5. Other electro-origami actuators. (**A**) Prebent electro-ribbon actuator that does not require preloading before actuation. (**B**) Electro-origami spiral that wraps around itself when actuated. (**C**) Electro-origami actuator inspired by spider silk, spooling around a central cylinder in the same manner that spider silk spools around liquid droplets [inset photographs provided by authors of (*32*)]. Scale bars, 20 mm.

Electro-origami materials

We initially investigated PET, polyimide tape, and PVC tape as insulators in an electro-origami fold test rig and confirmed that insulators with higher permittivities implied greater electrostatic forces (fig. S6), consistent with Eq. 1. Nonetheless, because of the simplicity of the electro-origami concept, any combination of conductive and insulating material can be used to manufacture useful devices. We cut strips of commercially available ITO-coated PET sheet and attached them together with cyanoacrylate adhesive to make an electro-ribbon actuator in minutes (Fig. 3C and movie S6A). Three-dimensional (3D)–printed electro-origami is also easily fabricated; we made an electro-ribbon actuator from 3D-printed graphene-loaded PLA and a 3D-printed

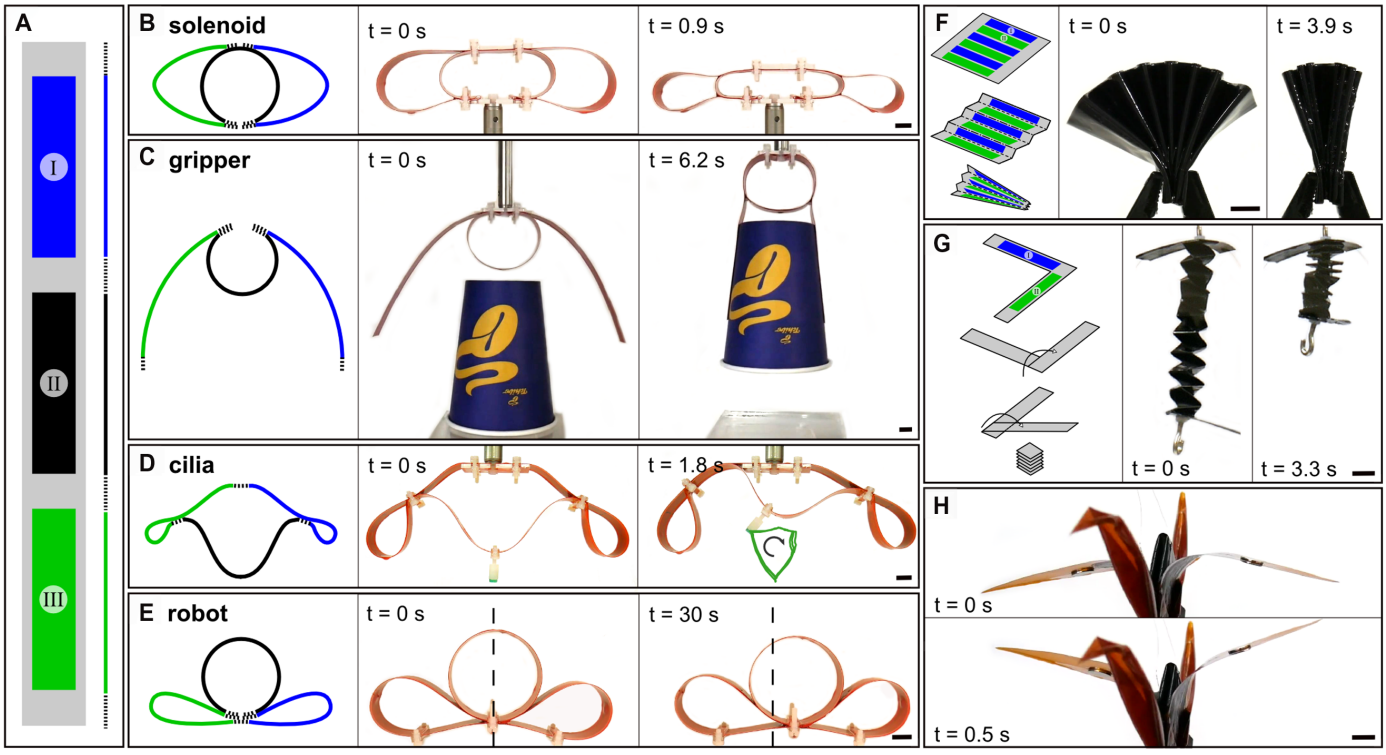

Fig. 6. Electro-origami devices. (**A**) Multifunctional electro-origami design, which can be used to make four unique functional devices. (**B**) Electro-origami solenoid actuator. (**C**) Electro-origami adaptive gripper, which also benefits from electroadhesive forces. (**D**) Electro-origami cilium structure, which drives a beam tip along a ciliate motion path. (**E**) Electro-origami locomotion robot, which can move left or right depending on the direction of sequential electrode charging. (**F**) Electro-origami fan that closes when activated. (**G**) Electro-origami muscle inspired by paper springs. (**H**) Electro-origami crane that flaps its wings when actuated. Scale bars, 10 mm.

pure PLA insulator (Fig. 3D and movie S6B). The insulator was a single 0.4-mm-thick 3D-printed layer of standard PLA filament that, once soaked in liquid dielectric, could withstand 10 kV. It is even possible to manufacture electro-origami devices with household or office materials. We used a normal (HB grade) pencil to draw graphite electrodes onto standard photocopier paper and joined the two layers together with cyanoacrylate adhesive to make a pencil-paper electro-ribbon actuator. After soaking in silicone oil, the 2-g paper actuator could lift 3 g through a stroke of 45 mm (Fig. 3E and movie S6C).

Electro-origami structures

Electro-ribbon actuators can also be easily integrated within multi-actuator structures to deliver higher forces and strokes. Stroke can be improved by stacking multiple actuators in series (Fig. 4A and movie S7A), and force can be increased by using a parallel arrangement (Fig. 4B and movie S7B). A lattice containing both series and parallel actuator elements allows for a balance between improved stroke and force (Fig. 4C and movie S7C). Bulk repetition of lattice structures will allow for the manufacture of self-actuating metamaterials powered by electro-origami across multiple scales.

Although the structures presented so far require external load to prime them for actuation, it is straightforward to manufacture prebent electro-ribbon actuators that do not require preloading (Fig. 5A and movie S8A). The electro-origami concept can be further extended to a wide range of electro-origami actuators. Figure 5B shows an electro-origami spiral, which consists of two insulated electrodes wrapped around an acrylic cylinder. When actuated, they wrap around one another, creating a tightly bound spiral of alternating electrodes (movie S8B). This arrangement can be used to make simple torsional actuators. An alternative arrangement of this structure takes inspiration from the tension-maintaining behavior of spider silk: We made an electro-origami spiral constrained at one electrode tip that spools around a central cylinder in the same manner that spider silk spools around liquid droplets (*32*), resulting in a large stroke of more than 60 cm (Fig. 5C and movie S8C). The maximum stroke of this design is only limited by electrode length.

Figure 6 (A to E) demonstrates the versatility of the electro-origami concept. With a single origami design featuring three electrodes in series (Fig. 6A), we were able to make four unique functional devices (movie S9) with origami folds and clips to hold the folds in place. First, we folded the design into a solenoid-like (self-restoring, linearly moving) actuator (Fig. 6B and movie S9A). The same design could be folded into an electro-origami adaptive gripper (Fig. 6C and movie S9B). Upon actuation, the gripper arms closed around the object to be gripped, with electroadhesive forces also improving grip strength, as in previously demonstrated electroadhesive dielectric elastomer grippers (*33*). More complex motions were achievable by charging electrodes sequentially: By attaching a beam to the same design, we were able to replicate the motion of a biological cilium, complete with a power and recovery stroke (Fig. 6D and movie S9C). Last, still using the same origami design, we were able to fold an electro-origami robot: Sequential electrode activation in one direction moved the robot to the right, and reversing the sequence moved the robot to the left (Fig. 6E and movie S9D).

Figure 6 (F and G) further shows electro-origami's potential real-world functionality. An electro-origami fan can be easily made from a

flat rectangular sheet with alternating electrodes. Alternating mountain and valley folds transform the sheet into a concertina shape, which may be pinched one end to produce a fan that closes when activated (Fig. 6F and movie S10A). This design could be used to create self-packing solar panels for space applications, with origami folding allowing compact packing as is achieved by tree leaves when packed inside buds (*34*). Figure 6G shows an electro-origami muscle made by alternately folding two insulated electrodes over one another. This artificial muscle exhibited more than 50% contraction (movie S10B), shortening by more than 4 cm in less than a second. Electro-origami artificial muscles could be used to replace or augment biological muscle in humanoid robots, prosthetics, and wearable devices.

Last, an origami crane was fabricated from polyimide film and painted with conducting ink electrodes on its wings and inside its body. Activation causes wing flexion resulting in a flapping motion (Fig. 6H and movie S10C). Combined with printable conductive inks, the electro-origami concept will allow inkjet-printed origami patterns that can be folded into functional devices.

DISCUSSION

Electro-origami is an actuation concept that exploits electrostatic attraction, high-permittivity, high–breakdown strength insulating fluids and dielectrophoresis to deliver powerful, versatile actuators and robotic devices. Although the number of active designs that electro-origami enables is very large, it is limited by the progressive zipping nature of the electro-origami concept—active devices that lack an origami fold to initiate zipping cannot be directly actuated. For these devices, discrete electro-origami actuators could be included to achieve motion. Another limitation of electro-origami is the high voltage required to develop strong electric fields. As with other state-of-the-art high-field actuators (*24*, *25*, *30*), an amplifier is needed to supply high voltage, which may introduce safety concerns for some applications. Nonetheless, the performance and versatility demonstrated here highlight the suitability of the electro-origami concept for a wide range of fields—including robotics, engineering, and transportation—and for applications such as deployable structures, space systems, and multiple degrees-of-freedom prostheses and robots.

MATERIALS AND METHODS

Manufacture of electro-origami folds

Figure S1A shows one way of making an electro-origami fold:

1) The electrodes and insulator are prepared. Wires can be soldered to the electrodes so that voltage can be applied. The insulator should be larger than the electrodes in the nonthickness directions to fully encapsulate it.

2) The electrodes are insulated with an insulator material, which also serves as the origami material to be folded. The figure shows insulation of the electrodes on both sides. In this case, the tape fully encapsulated the electrode to ensure that no arcing occurred. It is possible to insulate on the inner surface of the origami fold only; however, in this case, the insulation should be especially large in the nonthickness directions to prevent arcing.

3) The electro-origami is folded to prepare it for actuation.

Full submersion experiment

As part of the electro-origami concept, a small bead of liquid dielectric is added at the origami hinge, which considerably increases electrostatic force due to its higher breakdown strength and permittivity. A similar increase in tensile force could be achieved by submerging the whole device in liquid dielectric, but this would considerably increase mass and slow down movement because of opposing viscous and hydraulic forces. The liquid bead, in contrast, negligibly alters device mass and behavior but greatly increases force. We compared the difference in isometric tensile force between a fully submerged electro-ribbon actuator and one with only a bead of liquid dielectric at each origami hinge. The nonsubmerged actuator delivered 91.61% of the force of the submerged actuator, confirming the effectiveness of the electro-origami concept.

Electro-origami field strength distribution

The field strength distribution of electro-ribbon actuators is highly concentrated near the origami hinge. Figure S1B shows results from simulation using a field modeling software (QuickField, Tera Analysis Ltd., Denmark). The conductors are 30 mm in length, and the actuator is submerged in a medium with permittivity of 2.7, matching the silicone oil used in most experiments. The PVC tape permittivity is 4.62. The voltage between the upper and lower electrodes is 10 kV.

Derivation of electrostatic attractive force between two plates separated by an insulator and a medium

In electro-origami, an electrode and counterelectrode form a zipping structure. Between the electrodes are an insulator (which prevents short circuit) and a medium (which may be air or high-permittivity liquid dielectric). To shed light on the behavior of this system, we performed from-first-principles electrical analysis on an analogous system.

Consider two plates separated by two dielectric slabs of thicknesses $t_{\text{insulator}}$ and t_{medium} and permittivities $\varepsilon_{\text{insulator}}$ and $\varepsilon_{\text{medium}}$ (fig. S2A). They may be modeled as two variable capacitors in series whose capacitances are $C_{\text{insulator}}$ and C_{medium}. When a voltage V is applied across the two plates, they become charged. A virtual, infinitely thin plate at a voltage $V_{\text{interface}}$ may be assumed between the two dielectric slabs, where $V_{\text{interface}}$ is greater than zero but lower than V. The charge separated across the insulator dielectric slab, $Q_{\text{insulator}}$, is described by

$$Q_{\text{insulator}} = C_{\text{insulator}} V_{\text{interface}} \tag{4}$$

The charge separated across the medium dielectric slab, Q_{medium}, is described by

$$Q_{\text{medium}} = C_{\text{medium}} (V - V_{\text{interface}}) \tag{5}$$

Because the slabs are modeled as two capacitors in series, their charges are equivalent

$$Q_{\text{insulator}} = Q_{\text{medium}} \tag{6}$$

$$\therefore C_{\text{insulator}} V_{\text{interface}} = C_{\text{medium}} (V - V_{\text{interface}}) \tag{7}$$

$$\therefore V_{\text{interface}} = \frac{C_{\text{medium}}}{C_{\text{insulator}} + C_{\text{medium}}} V \tag{8}$$

The capacitance of the insulator and medium dielectric slabs is described by

$$C_{\text{insulator}} = \frac{\varepsilon_{\text{insulator}}\varepsilon_0 A}{t_{\text{insulator}}} \tag{9}$$

and

$$C_{\text{medium}} = \frac{\varepsilon_{\text{medium}}\varepsilon_0 A}{t_{\text{medium}}} \tag{10}$$

respectively. Substituting these into Eq. 8 leads to

$$V_{\text{interface}} = \frac{\varepsilon_{\text{medium}} t_{\text{insulator}}}{\varepsilon_{\text{insulator}} t_{\text{medium}} + \varepsilon_{\text{medium}} t_{\text{insulator}}} V \tag{11}$$

The energy $E_{\text{insulator}}$ stored across in insulator slab is given by

$$E_{\text{insulator}} = \frac{1}{2}\frac{\varepsilon_{\text{insulator}}\varepsilon_0 A {V_{\text{interface}}}^2}{t_{\text{insulator}}} \tag{12}$$

Differentiation of $E_{\text{insulator}}$ with respect to $t_{\text{insulator}}$ gives the force $F_{\text{insulator}}$ exerted at the interface.

$$F_{\text{insulator}} = -\frac{1}{2}\frac{\varepsilon_{\text{insulator}}\varepsilon_0 A {V_{\text{interface}}}^2}{{t_{\text{insulator}}}^2} \tag{13}$$

Substituting Eq. 11 results in

$$F_{\text{insulator}} = -\frac{1}{2}\frac{\varepsilon_{\text{insulator}}\varepsilon_0 A V^2}{\left(\frac{\varepsilon_{\text{insulator}}}{\varepsilon_{\text{medium}}} t_{\text{medium}} + t_{\text{insulator}}\right)^2} \tag{14}$$

An equal and opposite force is felt by the lower plate. Similarly, for the medium slab, the force F_{medium} exerted at the interface is

$$F_{\text{medium}} = \frac{1}{2}\frac{\varepsilon_{\text{medium}}\varepsilon_0 A (V - V_{\text{interface}})^2}{{t_{\text{medium}}}^2} \tag{15}$$

Substituting Eq. 11 results in

$$F_{\text{medium}} = \frac{1}{2}\frac{\varepsilon_{\text{medium}}\varepsilon_0 A V^2}{\left(\frac{\varepsilon_{\text{medium}}}{\varepsilon_{\text{insulator}}} t_{\text{insulator}} + t_{\text{medium}}\right)^2} \tag{16}$$

Unless the insulator and medium have the same permittivity, the forces exerted at the plates differ: The plate beside the material with the lower permittivity will experience a greater force. However, this does not imply that a net force acts to move the system through space; the resultant force acting on the plates is matched by an equal and opposite resultant force acting on the interface between the two dielectric slabs

$$\begin{aligned} F_{\text{interface}} &= F_{\text{insulator}} + F_{\text{medium}} \\ &= \frac{1}{2}\frac{\varepsilon_{\text{medium}}\varepsilon_{\text{insulator}}(\varepsilon_{\text{insulator}} - \varepsilon_{\text{medium}})\varepsilon_0 A V^2}{(\varepsilon_{\text{insulator}} t_{\text{medium}} + \varepsilon_{\text{medium}} t_{\text{insulator}})^2} \end{aligned} \tag{17}$$

In the case of electro-origami, the insulator is solid and firmly attached by adhesive to the insulator-adjacent plate, while the medium is liquid. Hence, we assume that the insulator and insulator-adjacent plate are inseparable and that the insulator is considerably stiffer than the (liquid) medium, such that its compression by $F_{\text{insulator}}$ is negligible, and it transmits any forces felt directly to the insulator-adjacent plate. This implies that the medium force F_{medium} will be exerted on both plates. Hence, the attractive force between the two plates is equal to F_{medium}

$$F = \frac{1}{2}\frac{\varepsilon_{\text{medium}}\varepsilon_0 A V^2}{\left(\frac{\varepsilon_{\text{medium}}}{\varepsilon_{\text{insulator}}} t_{\text{insulator}} + t_{\text{medium}}\right)^2} \tag{18}$$

Experimental validation of droplet volume model

We performed experiments to confirm the validity of the Euler-Bernoulli beam theory droplet volume model. An exact quantity of liquid dielectric was added by micropipette to an electro-origami fold hinge matching the one simulated by the model (fig. S1C). Applied voltage was gradually increased until pull-in occurred, and this pull-in voltage was recorded. Results show good agreement with those of the model (Fig. 1C).

Manufacture of electro-ribbon actuators

Figure 1F shows one way of making an electro-ribbon actuator:

1) The electrodes and insulator are prepared. Wires can be soldered to the electrodes so that voltage can be applied. The insulator should be larger than the electrodes in the nonthickness directions to fully encapsulate it.

2) One or both electrodes are insulated with the insulator material. The figure shows insulation of the upper electrode on both sides. In this case, the tape fully encapsulates the electrode to ensure that no arcing will occur. It is also possible to insulate both electrodes. Alternatively, insulation can only consist of the central insulating layer; in this case, it should be especially large in the nonthickness directions to prevent arcing around it.

3) Connections at the ends of the actuator are made to create two origami hinges and hold the actuator together under high load. Connections can be made using any connection method, such as adhesive, magnetic, or mechanical. During experiments, we used cyanoacrylate or epoxy adhesive, single magnets (because some electrodes were magnetic), or magnet pairs or mechanical clips, including insulated bulldog clips or custom acrylic clips held in place by plastic nuts and bolts.

4) The actuator is complete and can be extended by application of a central load. A liquid dielectric bead may be added at each origami hinge, and application of high voltage will cause exertion of force and contraction.

Reported electro-ribbon actuators

Throughout the main text, we avoid describing the specifications of example actuators in detail for reasons of brevity and instead refer to example actuators based on their qualities, for example, the "standard" and the "high-stress" electro-ribbon actuator. These actuators are made from of steel strips insulated with PVC tape. The dimensions of the steel strips used to fabricate them, along with their masses, contractions, and descriptions, are shown in Table 1.

Test protocol for isometric and isotonic experiments

During isometric testing, an electronic ribbon actuator was held at various actuator extensions (fig. S4C). The upper central point of the actuator was attached to a load cell (DBCR-10N-002-000, Applied Measurements Ltd., UK), which was attached to a rigid frame. The lower central point of the actuator was attached to a precision jack stand, which could be used to adjust actuator extension. Extension was recorded with a laser displacement meter (LK-G402, Keyence, Japan), which measured the displacement of the top of the jack stand. Application of high voltage caused electrostatic attraction and zipping, resulting in a tensile force at the center of the actuator, which was measured by the load cell. Liquid dielectric was added by pipette to the actuator's origami hinges.

During isotonic testing, the upper central point of the actuator was attached to a rigid frame (fig. S4C). A known mass was attached to the lower central point of the actuator, exerting a constant vertical load and causing actuator extension. Actuator contraction was recorded with a laser displacement meter, which measured the displacement of the test mass. For each trial, liquid dielectric was added by pipette to the actuator's origami hinges, and high voltage was applied until actuation was completed.

Variation between samples of standard electro-ribbon actuator

To investigate variation between actuator samples, we fabricated five standard electro-ribbon actuators and performed isometric tests at actuator extensions of 1, 2, and 4 mm. Figure S4 (D and E) shows tensile force variation with voltage and extension: Points are averages of five trials of five samples (25 total trials), and error bars show ±1 SD between averages of five trails for each sample (five samples). Maximum SD for liquid dielectric data was 0.2475 N at 6 kV.

Bandwidth testing

We performed bandwidth testing to determine the frequencies of operation that electro-origami could deliver. A standard electro-ribbon actuator (table S2) was modified by the addition of a small mechanical stop. This stop slightly reduced the maximum contraction but limited the adhesive and cohesive forces associated with the liquid dielectric when the actuator fully closed, allowing for higher-frequency repeating operation. At a voltage of 7 kV, this actuator was capable of full actuation and relaxation at a bandwidth of 0.125 Hz. If full contraction is not required, such that lower stroke is allowed, and bandwidth is less influenced by adhesive and cohesive forces, then much higher bandwidths can be achieved; 5 and 10 Hz are demonstrated using 7 kV (Fig. 2C and movie S3).

Cyclic testing

Cyclic testing was performed to determine the effects of long-term continuous reciprocating use of electro-origami devices. A 30-mm-long, 12.7-mm-wide electro-ribbon actuator with 50-μm-thick electrodes was modified with multiple parallel channel-shaped cutouts in the insulator layer, aligned perpendicularly to actuator's long axis, which acted as liquid reservoirs to retain liquid dielectric during the cyclic experiment. The actuator was stimulated with a 50% duty cycle square voltage wave of amplitude 8 kV at a frequency of 4 Hz. There was negligible variation in isometric force over 100,000 cycles (Fig. 2D), and after 100,000 cycles, the force exerted was 8.706 times greater than the force exerted by the same actuator with no liquid dielectric present. This demonstrates how features such as surface structure modifications can be used to ensure retention of liquid dielectric for long-term operation of electro-origami devices. Surface structure (including surface roughness) can affect the behavior of the liquid dielectric and the electric field generated and thus the behavior of electro-origami devices.

Measurement of energetic efficiency

To measure energy efficiency, we used data recorded from experiments. The high-voltage amplifiers (5HVA24-BP1, UltraVolt, USA) provided monitor voltage outputs corresponding to delivered high voltage and current. These monitor voltages were recorded with a data acquisition device (NI USB-6343, National Instruments, USA) and converted to units of volts and amperes. The product of the inferred voltage and current was the electrical power. To determine electrical energy consumed, we numerically integrated electrical power with the MATLAB "trapz" function as an actuator lifted a load. Because the voltage when the actuator was relaxing was zero, the power was also zero at this time, and only the electrical power when the actuator was shortening was considered. Mechanical energy output was calculated according to gravitational potential energy, i.e., GPE = mgh, where GPE is gravitational potential energy, m is mass, g is local acceleration due to gravity, and h is stroke. Efficiency was calculated as mechanical energy output divided by electrical energy consumed.

Efficiency varied between experiments, and the greatest variation was a function of which insulation was used. For example, PVC tape, which has a comparatively low resistivity (10^{12} to 10^{14} ohm·m), resulted in a noticeable leakage current, which consumed electrical energy without providing any mechanical energy, resulting in lower efficiencies. With PVC insulation, maximum leakage current when 6 kV was applied was 21.74 μA, implying a leakage current per unit area of 17.12 mA m^{-2} (electrode dimensions were 100 mm by 12.7 mm). In contrast, in experiments where polyimide tape was used (resistivity on the order of 10^{15} ohm·m), maximum leakage current was around 0.2 μA, implying a leakage current per unit area of 0.16 mA m^{-2}. Hence, less energy was lost to leakage, and efficiency was considerably higher. The trial with the greatest efficiency involved a standard electro-origami actuator, insulated with two layers of polyimide tape, lifting a 3 g mass while actuated by an applied voltage of 6 kV. The stroke was 51.7 mm, implying an output mechanical energy of 1.5215 mJ. The consumed electrical energy calculated with the MATLAB trapz function was 2.1839 mJ. Therefore, the efficiency was calculated as 69.67%. Figure 2E shows applied voltage, delivered current, and electrical power traces during the experiment in question.

Simulating the effect of morphology on output parameter

Euler-Bernoulli beam theory becomes less accurate as deflections increase. The developed MATLAB model can be used with larger tip loads that induce greater deflections; however, the diminishing accuracy of results as tip load increases should be considered. Nonetheless, results can provide qualitative support for experimental findings. The developed model was used to investigate the effect of morphology (electrode thickness, length, and width) on output parameters (maximum load lifted and maximum stroke) for comparison with experimental results (Fig. 2, G to I). The simulated electrode had the following standard properties: thickness, 50 μm; length, 100 mm; width, 12.7 mm; and Young's modulus, 190 GPa (matching those of the standard electro-ribbon actuator).

Calculation of performance characteristics for electro-ribbon actuators

Actuator thickness was calculated assuming two electrodes (using steel strip thickness) and one insulator, the insulator being composed of two layers of PVC tape. This was the number of layers used to make most actuators (the insulator could have been composed of a single layer of PVC tape but would not be able to withstand 10 kV). Similarly, actuator mass was the combined mass of the conductors and insulator. Detailed characteristics of the electro-ribbon actuators in question are available in Table 1.

Actuator force was determined differently depending on the type of experiment. For isotonic experiments, actuator force was the weight of the load lifted. For isometric experiments, actuator force was recorded using a load cell (DBCR-10N-002-000, Applied Measurements Ltd., UK). Maximum achieved actuator force was 12.91 N using the high-force actuator, which lifted 1.316 kg.

Stress was calculated as actuator force divided by maximum actuator cross-sectional area, which was steel strip free length multiplied by steel strip width. The highest achieved stress was achieved with an actuator 10 mm in length and 12.7 mm in width, implying a maximum cross-sectional area of 127 mm^2. This actuator lifted a maximum load of 527.75 g, implying a force of 5.1772 N. These imply a stress of 40.77 kPa.

Specific force was calculated as actuator force divided by actuator mass. The highest achieved specific force was 10164.25 N kg^{-1} with the high–specific force actuator, which lifted 373 g despite having a mass of only 0.36 g, lifting more than 1036 times its own mass.

Stroke was the distance traveled during actuation, typically recorded using a laser displacement meter (LK-G402, Keyence, Japan). Contraction was calculated as stroke divided by initial actuator length, which was equal to stroke divided by the sum of stroke and actuator thickness. The highest achieved contraction was achieved by an actuator featuring 20-μm-thick electrodes, implying an actuator thickness of 300 μm (two 20-μm-thick electrodes and two 130-μm-thick insulator layers). The stroke was 181.92 mm, implying an initial actuator length of 182.22 mm. This implied a contraction of 99.84%.

Contraction rate was calculated as actuator speed divided by initial actuator length. The highest recorded contraction rates were achieved during power measurement experiments (Fig. 2F and movie S5). As the mass traveled upward, it traveled 5.0869 mm in 0.073 s, implying an average speed of 69.6835 mm s^{-1}. The actuator's initial length was 6 mm, implying an average contraction rate of 1161% s^{-1}. The actuator's peak speed as the mass traveled upward was 119.1121 mm s^{-1}, implying a peak contraction rate of 1985% s^{-1}.

Stroke mechanical energy was calculated as the change in gravitational potential energy associated with stroke, equal to the product of mass, stroke, and local gravitational acceleration. Power was calculated as the sum of the time derivatives of potential energy and kinetic energy. The time derivative of potential energy was calculated as $\frac{d}{dt}(mgh) = mgv$, where m was mass, g was local acceleration due to gravity, h was mass position, and v was mass velocity. The time derivative of kinetic energy was calculated as $\frac{d}{dt}\left(\frac{1}{2}mv^2\right) = mva$, where a was mass acceleration. Hence, power was calculated as $mgv + mga$.

Specific energy was calculated as stroke mechanical energy divided by actuator mass, and specific power was calculated as power divided by actuator mass. The highest recorded specific energy was achieved by an actuator of mass 2.28 g, which lifted a 27.75-g load through a stroke of 57.63 mm, implying a stroke mechanical energy of 15.6885 mJ, which implies a specific energy of 6.8809 J kg^{-1}. The highest recorded specific power was achieved by an actuator of mass 13.2 g, which oscillated a 1033-g mass at a frequency of 6.9 Hz (Fig. 2F and movie S5). The average and peak powers were 0.6792 and 1.3663 W, implying average and peak specific powers of 51.45 and 103.51 W kg^{-1}, respectively.

Energy density was calculated as stroke mechanical energy divided by actuator volume. Power density was calculated as power divided by actuator volume. The highest recorded energy density was achieved with an actuator 10 mm in length and 12.7 mm in width, featuring two 50-μm-thick electrodes and two layers of 130-μm-thick insulator, implying a volume of 45.72 mm^3. This actuator lifted a 257.3-g load through a stroke of 0.8 mm, implying a stroke mechanical energy of 2.0193 mJ, which implies an energy density of 44.17 kJ m^{-3}. The highest power density was achieved by the same actuator with the highest recorded specific power, which was 100 mm in length and 12.7 mm in width, and featured two 500-μm-thick electrodes and two layers of 130-μm-thick insulator, implying a volume of 1600.2 mm^3. The average and peak powers were 0.6792 and 1.3663 W, implying average and peak power densities of 424.45 and 853.83 kW m^{-3}, respectively.

The dimensions, masses, and contractions of actuators achieving maximum performance characteristics are presented in Table 1. In general, long actuators with thin electrodes were more compliant and deflected further under load, implying high strokes. In contrast, short actuators with thick electrodes were stiffer and deflected less under load, implying increased electric fields and consequently greater forces. To maximize actuation stress, short actuators were also advantageous because they maximized the amount of "active" actuator area; in long actuators that progressively zip, only a small fraction of the actuator area is contributing a large electrostatic force. For performance metrics that are a function of both force and stroke, such as specific energy and power density, intermediate values of actuator length and thickness resulted in the best performance.

Insulator material investigation using an electro-origami fold test rig

We investigated the electro-origami concept using a simple test rig (fig. S1C). The test rig consisted of an upper electrode (a 70-μm-thick, 12.7-mm-wide steel strip) that was attached with adhesive to an acrylic plate. The upper electrode was insulated with one of several insulator materials. A second electrode (a 70-μm-thick, 12.7-mm-wide steel strip with free length of 100 mm) was fixed at one end adjacent to the insulated electrode. Application of a test mass to the tip of the second electrode caused cantilever deflection. Application of a bead of liquid dielectric and high voltage caused electrostatic zipping, raising the test mass against gravity.

We investigated the maximum load lifted, with the insulator being PET, polyimide tape, or PVC tape. The permittivity of PET is typically stated as between 3 and 3.4, that of polyimide tape as between 3.4 and 3.5, and that of PVC tape used as 4.62 (personal communication, Advance Tapes). The thickness of the insulator layer was conserved, and the dominant contributor to flexural rigidity was the steel electrode, so the behavior was purely a function of electrical properties. Results showed that maximum load lifted increased monotonically with insulator permittivity (fig. S6, C and D), as predicted by eq. S14.

Multiactuator structures

The standard electro-ribbon actuator could lift a 26-g mass through a stroke of 57.63 mm. Two standard electro-ribbon actuators in series could lift a 22-g mass through a stroke of 109.90 mm. Two standard

electro-ribbon actuators in parallel could lift a 38-g mass through a stroke of 67.42 mm. The lattice of standard electro-ribbon actuators could lift a 26-g mass through a stroke of 107.24 mm.

SUPPLEMENTARY MATERIALS

robotics.sciencemag.org/cgi/content/full/3/25/eaau9795/DC1
Materials and Methods
Fig. S1. Manufacture, field strength distribution, and experimental test setup of electro-origami fold.
Fig. S2. Models used to derive electrostatic force.
Fig. S3. Flowchart showing structure of a recursive MATLAB script.
Fig. S4. Characterization and analysis of electro-ribbon actuator.
Fig. S5. Results from electro-origami fold simulation.
Fig. S6. Effect of material properties on performance of electro-origami fold.
Table S1. Summary of materials used for electro-origami.
Movie S1. An electro-origami fold.
Movie S2. Isotonic and isometric actuation of a standard electro-ribbon actuator.
Movie S3. Bandwidth testing of a standard electro-ribbon actuator.
Movie S4. High-stress and high-contraction electro-ribbon actuators.
Movie S5. High-power electro-ribbon actuator.
Movie S6. Manufacture and testing of electro-ribbon actuators made from different materials.
Movie S7. Series, parallel, and lattice arrangements of standard electro-ribbon actuators.
Movie S8. Electro-origami actuators.
Movie S9. Four electro-origami devices from one electro-origami design.
Movie S10. Complex electro-origami devices.

REFERENCES AND NOTES

1. P. W. K. Rothemund, Folding DNA to create nanoscale shapes and patterns. *Nature* **440**, 297–302 (2006).
2. H. Liu, R. M. Crooks, Three-dimensional paper microfluidic devices assembled using the principles of origami. *J. Am. Chem. Soc.* **133**, 17564–17566 (2011).
3. Z. Song, T. Ma, R. Tang, Q. Cheng, X. Wang, D. Krishnaraju, R. Panat, C. K. Chan, H. Yu, H. Jiang, Origami lithium-ion batteries. *Nat. Commun.* **5**, 3140 (2014).
4. A. M. Hoover, R. S. Fearing, Fast scale prototyping for folded millirobots, in *2008 IEEE International Conference on Robotics and Automation*, Pasadena, CA, USA, 19 to 23 May 2008 (IEEE, 2008), pp. 1777–1778.
5. K. Miura, Map fold a la Miura style, its physical characteristics and application to the space science, in *Research of Pattern Formation* (KTK Scientific Publishers, 1994), pp. 77–90.
6. K. Kuribayashi, K. Tsuchiya, Z. You, D. Tomus, M. Umemoto, T. Ito, M. Sasaki, Self-deployable *origami* stent grafts as a biomedical application of Ni-rich TiNi shape memory alloy foil. *Mater. Sci. Eng. A* **419**, 131–137 (2006).
7. R. V. Martinez, C. R. Fish, X. Chen, G. M. Whitesides, Elastomeric origami: Programmable paper-elastomer composites as pneumatic actuators. *Adv. Funct. Mater.* **22**, 1376–1384 (2012).
8. S. Li, D. M. Vogt, D. Rus, R. J. Wood, Fluid-driven origami-inspired artificial muscles. *Proc. Natl. Acad. Sci. U.S.A.* **114**, 13132–13137 (2017).
9. J. K. Paik, B. An, D. Rus, R. J. Wood, Robotic origamis: Self-morphing modular robots, in *Proceedings of the 2nd International Conference on Morphological Computation*, Venice, 12 to 14 September 2011 (ICMC, 2011), pp. 29–31.
10. S. M. Felton, M. T. Tolley, B. Shin, C. D. Onal, E. D. Demaine, D. Rus, R. J. Wood, Self-folding with shape memory composites. *Soft Matter* **9**, 7688–7694 (2013).
11. E. Smela, O. Inganäs, I. Lundström, Controlled folding of micrometer-size structures. *Science* **268**, 1735–1738 (1995).
12. D. Pugal, K. Jung, A. Aabloo, K. J. Kim, Ionic polymer–metal composite mechanoelectrical transduction: Review and perspectives. *Polym. Int.* **59**, 279–289 (2010).
13. R. P. Feynman, R. B. Leighton, M. Sands, *The Feynman Lectures on Physics, Vol. II: Mainly Electromagnetism and Matter* (Addison-Wesley, 1979).
14. W. C. Tang, T.-C. H. Nguyen, R. T. Howe, Laterally driven polysilicon resonant microstructures. *Sens. Actuators* **20**, 25–32 (1989).
15. H. Conrad, H. Schenk, B. Kaiser, S. Langa, M. Gaudet, K. Schimmanz, M. Stolz, M. Lenz, A small-gap electrostatic micro-actuator for large deflections. *Nat. Commun.* **6**, 10078 (2015).
16. K. Sato, M. Shikida, Electrostatic film actuator with a large vertical displacement, in *[1992] Proceedings IEEE Micro Electro Mechanical Systems*, Travemunde, Germany, Germany, 4 to 7 February 1992 (IEEE, 1992), pp. 1–5.
17. J. Branebjerg, P. A. Gravesen, A new electrostatic actuator providing improved stroke length and force, in *[1992] Proceedings IEEE Micro Electro Mechanical Systems*, Travemunde, Germany, 4 to 7 February 1992 (IEEE, 1992), pp. 6–11.
18. M. Elwenspoek, L. Smith, B. Hok, Active joints for microrobot limbs. *J. Micromech. Microeng.* **2**, 221–223 (1992).
19. L. Maffli, S. Rosset, H. R. Shea, Zipping dielectric elastomer actuators: Characterization, design and modeling. *Smart Mater. Struct.* **22**, 104013 (2013).
20. A. S. Chen, H. Zhu, Y. Li, L. Hu, S. Bergbreiter, A paper-based electrostatic zipper actuator for printable robots, in *2014 IEEE International Conference on Robotics and Automation (ICRA)*, Hong Kong, China, 31 May to 7 June 2014 (ICRA, 2014), pp. 5038–5043.
21. J. Li, H. Godaba, Z. Q. Zhang, C. C. Foo, J. Zhu, A soft active origami robot. *Extreme Mechanics Letters* **24**, 30–37 (2018).
22. K. Sarabandi, L. Pierce, An overview of research in advanced microelectronics for micro-autonomous platforms, in *Proceedings of SPIE—The International Society for Optical Engineering*, Orlando, Florida, United States, 13 to 17 April 2009 (SPIE, 2009), pp. 73180M.
23. M. Gaudet, S. Uhlig, M. Stolz, S. Arscott, H. Conrad, S. Langa, B. Kaiser, H. Schenk, Electrostatic bending actuators with a liquid filled nanometer scale gap, in *2017 IEEE 30th International Conference on Micro Electro Mechanical Systems (MEMS)*, Vegas, Nevada, USA, 22 to 26 January 2017 (MEMS, 2017), pp. 175–178.
24. E. Acome, S. K. Mitchell, T. G. Morrissey, M. B. Emmett, C. Benjamin, M. King, M. Radakovitz, C. Keplinger, Hydraulically amplified self-healing electrostatic actuators with muscle-like performance. *Science* **359**, 61–65 (2018).
25. N. Kellaris, V. Gopaluni Venkata, G. M. Smith, S. K. Mitchell, C. Keplinger, Peano-HASEL actuators: Muscle-mimetic, electrohydraulic transducers that linearly contract on activation. *Sci. Robot.* **3**, eaar3276 (2018).
26. Z. Suo, Theory of dielectric elastomers. *Acta Mech. Solida Sin.* **23**, 549–578 (2010).
27. H. A. Pohl, The motion and precipitation of suspensoids in divergent electric fields. *J. Appl. Phys.* **22**, 869–871 (1951).
28. H. Pellat, Électrostatique non fondée sur les lois de coulomb. Forces agissant sur les diélectriques non électrisés. *J. Phys. Theor. Appl.* **5**, 244–256 (1896).
29. P. Brochu, Q. Pei, Advances in dielectric elastomers for actuators and artificial muscles. *Macromol. Rapid Commun.* **31**, 10–36 (2010).
30. J. D. W. Madden, N. A. Vandesteeg, P. A. Anquetil, P. G. A. Madden, A. Takshi, R. Z. Pytel, S. R. Lafontaine, P. A. Wieringa, I. W. Hunter, Artificial muscle technology: Physical principles and naval prospects. *IEEE J. Oceanic Eng.* **29**, 706–728 (2004).
31. G. Kovacs, L. Düring, S. Michel, G. Terrasi, Stacked dielectric elastomer actuator for tensile force transmission. *Sens. Actuators A Phys.* **155**, 299–307 (2009).
32. H. Elettro, S. Neukirch, F. Vollrath, A. Antkowiak, In-drop capillary spooling of spider capture thread inspires hybrid fibers with mixed solid–liquid mechanical properties. *Proc. Natl. Acad. Sci. U.S.A.* **113**, 6143–6147 (2016).
33. J. Shintake, S. Rosset, B. Schubert, D. Floreano, H. Shea, Versatile soft grippers with intrinsic electroadhesion based on multifunctional polymer actuators. *Adv. Mater.* **28**, 231–238 (2016).
34. H. Kobayashi, B. Kresling, J. F. V. Vincent, The geometry of unfolding tree leaves. *Proc. Biol. Sci.* **265**, 147–154 (1998).

Acknowledgments: Funding: M.T. was supported by EPSRC grant EP/M026388/1 and EP/R02961X/1. T.H. was supported by EPSRC grant EP/M026388/1 and the Royal Academy of Engineering and the Office of the Chief Science Adviser for National Security under the UK Intelligence Community Postdoctoral Fellowship Programme. J.R. was supported by EPSRC grants EP/L015293/1, EP/M020460/1, and EP/M026388/1 and the Royal Academy of Engineering through the Chair in Emerging Technologies scheme. **Author contributions:** M.T., T.H., and J.R. jointly conceived of electro-origami and all device concepts. M.T. and T.H. designed the experiments, manufactured the devices, collected the data, performed the analysis, interpreted the results, wrote the manuscript, and created the movies. J.R. advised on all parts of the project and reviewed the manuscript. **Competing interests:** The authors declare that they have no competing interests. Two patent applications have been filed relating to this work by the University of Bristol: UK patent application no. GB1710400.1 on 29 June 2017 and international patent application no. PCT/GB2018/051799 on 29 June 2018. **Data and materials availability:** All data needed to evaluate the conclusions in the paper are present in the paper or the Supplementary Materials. The datasets generated and analyzed during the current study are available in the University of Bristol Research Data Repository (https://data.bris.ac.uk/data/): 10.5523/bris.1qreev788jlm82cvgytvm4cuoo. Requests for materials should be addressed to J.R.

Submitted 2 August 2018
Accepted 16 November 2018
Published 19 December 2018
10.1126/scirobotics.aau9795

Citation: M. Taghavi, T. Helps, J. Rossiter, Electro-ribbon actuators and electro-origami robots. *Sci. Robot.* **3**, eaau9795 (2018).

Science Robotics

Electro-ribbon actuators and electro-origami robots

Majid Taghavi, Tim Helps, and Jonathan Rossiter

Sci. Robot. **3** (25), eaau9795. DOI: 10.1126/scirobotics.aau9795

Science Robotics (ISSN 2470-9476) is published by the American Association for the Advancement of Science. 1200 New York Avenue NW, Washington, DC 20005. The title *Science Robotics* is a registered trademark of AAAS.